

S. Tanaka · H. Suzuki · S. Sadamoto · S. Okazawa ·
T.T. Yu · T.Q. Bui

Accurate evaluation of mixed-mode intensity factors of cracked shear-deformable plates by an enriched meshfree Galerkin formulation

Received: date / Accepted: date

Abstract A novel meshfree discretization technique in terms of the reproducing kernel particle method is presented for accurately evaluating mixed-mode intensity factors of cracked shear-deformable plates. Mindlin-Reissner plate theory is adopted to solve the cracked plates problem in the Galerkin formulation, considering transverse shear deformation. The diffraction method, visibility criterion and enriched basis are included in the generation of meshfree interpolants for the modeling of fracture. In this work, numerical integration is treated using the stabilized conforming nodal integration (SCNI) and subdomain stabilized conforming integration (SSCI). The J -integral (contour integral) is employed to analyze the fracture mechanics parameters. SCNI/SSCI are thus adopted to evaluate the contour integral and to split the original J -integral into symmetric and asymmetric J -integral values. They are calculated by decomposing the smoothed displacement, moment and shear force quantities into symmetric/asymmetric parts. In addition, a displacement ratio method is introduced to divide the asymmetric J -integral value into corresponding moment and shear force intensity factors. The accuracy of the intensity factors and the path-independent properties in mixed-mode fracture problems are critically examined through several numerical examples.

Keywords Meshfree, Reissner-Mindlin Plate, Fracture, J -integral, Nodal Integration

S.Tanaka, H.Suzuki, S.Sadamoto
Graduate School of Engineering, Hiroshima University, 4-1, Kagamiyama 1-chome, Higashi-Hiroshima,739-8527, Japan
Tel.: +81-82-424-7859
Fax: +81-82-422-8527
E-mail: satoyuki@hiroshima-u.ac.jp
H.Suzuki
E-mail: m140825@hiroshima-u.ac.jp
S.Sadamoto
E-mail: shota.sadamoto@gmail.com

S.Okazawa
Division of Mechanical Engineering, Faculty of Engineering, University of Yamanashi, Japan
E-mail: sokazawa@yamanashi.ac.jp

T.T.Yu
Department of Engineering Mechanics, Hohai University, China
E-mail: tiantangyu@hhu.edu.cn

T.Q.Bui
Department of Civil and Environmental Engineering, Tokyo Institute of Technology, Japan
E-mail: tinh.buiquoc@gmail.com

1 Introduction

Ships and ocean structures are generally composed of steel plate structures. The structures are joined for example by welding, and it is possible that flaws may occur in the weld part during manufacturing process or in-service once suffering external loading conditions. Fatigue and fracture phenomena of welded steel structures have been comprehensively summarized (e.g., Maddox [1]; Suresh [2]; Fricke [3]; Anderson [4]). In a typical case of the fracture of a ship's hull, initial defects form and coalesce around the weld part, producing a semi-elliptical flaw. The surface flaw develops through-the-thickness cracks (through cracks) under cyclic loadings. Additionally, the cracks occasionally propagate along the weld line, from the plate to stiffeners, and from the plate to structural members; e.g., longitudinal girders, transverse frames and outer shells. Damage to main members reduces the load carrying capacity of the hull structure. It is important to design such marine structures appropriately so that large-scale fracture accidents can be avoided according to the concept of damage tolerance. Studies have evaluated fatigue and fracture problems for steel structures (e.g., Toyosada et al. [5-6]; Okawa et al. [7]; Sumi et al. [8]; He et al. [9]; Qiao et al. [10]). However, challenging tasks remain in analyzing fracture behaviors, crack trajectories and fatigue cycles in cracked plate structures, and in the modeling of a fracture.

The shell finite element method (FEM) is an effective means proposed for analyzing very thin and very large structures, such as a ship's hull (e.g., Yao and Fujikubo [11]). The FEM is thus well suited to treating a fracture with shell elements. The shell modeling is generally formulated according to the combination of the plane stress condition and plate bending theory. Although many studies of fracture mechanics have analyzed two-dimensional (2D) plane stress condition [4], there are a few fracture mechanics analyses of plate bending formulations (e.g., Kirchhoff-Love theory and Mindlin-Reissner theory), relative to the number of 2D fracture mechanics analyses. Among them, Hui and Zehnder [12], Young and Sun [13], Viz et al. [14] and Su and Leung [15] analyzed the fracture of plates and the moment/shear force intensity factors. Dirgantara and Aliabadi [16] dealt with cracks in thin plates by employing a dual-boundary element method [17]. Dolbow et al. [18] numerically investigated mixed-mode cracked plates by employing the extended FEM [19]. Wang et al. [20] formulated a boundary collocation method for cracked plates analysis. Zehnder and Viz [21] summarized fracture mechanics in thin plates and shells under different loading conditions. A cracked thin shell analysis was carried out in [22] by isogeometric analysis [23-27]. The moment and shear force intensity factors for several crack configurations and combinations of loading conditions were presented by Sih [28] and Murakami [29]. It is necessary to extract moment/shear force intensity factors from the J -integral predicting crack propagation phenomena in a shell structure [30-31]. In spite of the success and the variety of existing numerical methods for evaluation of mixed-mode intensity factors in cracked plates, there is still a growing interest in the development of new methods.

A novel discretization technique in terms of a meshfree Galerkin formulation for analyzing the mixed-mode intensity factors in cracked shear-deformable plates is presented. The reproducing kernels (RKs) (Liu et al. [32]) are adopted as interpolation functions, and the meshfree Mindlin-Reissner plate formulation (Wang and Chen [33]; Wang and Sun [34]; Sadamoto et al. [35]) is used. A diffraction method, visibility criterion (Organ et al. [36]; Krysl and Belytschko [37]) and enriched basis (Fleming et al. [38]; Joyot et al. [39]) are included for the RKs to represent the asymptotic field near the crack tip in the meshfree modeling. The stiffness matrix is numerically integrated by employing stabilized conforming nodal integration (SCNI) (Chen et al. [40-41]) and subdomain stabilized nodal integration (SSCI) (Wang and Chen [42]; Wang and Lin [43-45]; Tanaka et al. [46]; Wang and Peng [47]). The mixed-mode intensity factors are evaluated using the J -integral (contour integral), which is discretized based on the nodal integration techniques. The contour integral is decomposed into symmetric and asymmetric J -integral values by splitting the displacement, moment and shear force quantities into line symmetric and asymmetric parts across the crack segments. In addition, a displacement ratio is employed to extract the corresponding moment and shear force intensity factors from the asymmetric J -integral value according to an idea presented by Rigby and Aliabadi [48] and Dirgantara and Aliabadi [30].

In a previous study, Tanaka et al. [49] evaluated the 2D in-plane mixed-mode stress intensity factors (SIFs) using a decomposition method based on meshfree modeling, and obtained high-accuracy of the SIFs and a path-independent property. The decomposition method and meshfree discretization are thus extended to the plate bending formulation when evaluating mixed-mode intensity factors.

Although a purely mode-I moment intensity factor was analyzed under several model configurations and loading conditions by Tanaka et al. [50], adoption of the decomposition method and displacement ratio method for the evaluations of the mixed-mode moment/shear force intensity factor in meshfree crack modeling has not been reported in the literature yet. The present paper conducts a meshfree discretization for mixed-mode crack problems, evaluating the intensity factors, and critically examining the path-independent properties through a series of representative numerical examples.

The remainder of the paper is organized as follows. Section 2 describes the Mindlin-Reissner plate formulation, crack modeling and discretization employing the meshfree Galerkin method. Section 3 presents the evaluation of the J -integral, and a technique used to separate the mixed-mode intensity factors. Numerical examples for mixed-mode crack problems are presented in Section 4. Concluding remarks are given in Section 5.

2 A meshfree Galerkin formulation for shear-deformable plates

2.1 Mindlin-Reissner plate theory

Let us consider a shear-deformable plate containing a through crack shown in Fig.1a assuming that the material under a low strain condition is isotropic and elastic. The rectangular plate is embedded in a Cartesian coordinate system $(x_1-x_2-x_3)$. The middle section of the cracked plate and its boundary are denoted S and ∂S , respectively. The through crack ∂S_c is embedded in the plate. S_+/S_- represent the upper/lower regions of the through crack. The plate thickness is t .

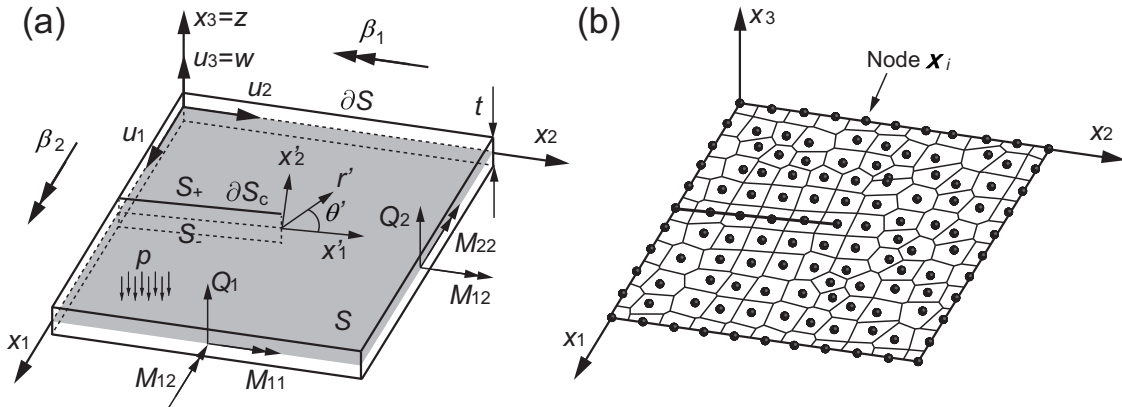


Fig. 1 Boundary value problem for a cracked shear-deformable plate: **a** A shear-deformable plate including a through crack, **b** a meshfree discretization for the cracked plate

The displacement vector $\mathbf{u}(\mathbf{x})$ in the shear-deformable plate can be written as:

$$\mathbf{u}(\mathbf{x}) = \begin{Bmatrix} u_1(\mathbf{x}) \\ u_2(\mathbf{x}) \\ u_3(\mathbf{x}) \end{Bmatrix} = \begin{Bmatrix} -z\beta_1(\mathbf{x}) \\ -z\beta_2(\mathbf{x}) \\ w(\mathbf{x}) \end{Bmatrix}, \quad (1)$$

where $\beta_1(\mathbf{x})(=\beta_1)$ and $\beta_2(\mathbf{x})(=\beta_2)$ are the rotational components. $w(\mathbf{x})(=w)$ is a deflection component. In the shear-deformable plate theory, the vector form of the strain components $\boldsymbol{\varepsilon}$ can be decomposed into shear strain and bending deformation components $\boldsymbol{\varepsilon}^b$ and $\boldsymbol{\varepsilon}^s$, i.e., $\boldsymbol{\varepsilon} = \{\boldsymbol{\varepsilon}^b \ \boldsymbol{\varepsilon}^s\}^T$.

The components can be written as:

$$\begin{aligned}\boldsymbol{\varepsilon}^b &= \begin{Bmatrix} \varepsilon_{11} \\ \varepsilon_{22} \\ 2\varepsilon_{12} \end{Bmatrix} = \begin{Bmatrix} -z \frac{\partial \beta_1}{\partial x_1} \\ -z \frac{\partial \beta_2}{\partial x_2} \\ -z \left(\frac{\partial \beta_2}{\partial x_1} + \frac{\partial \beta_1}{\partial x_2} \right) \end{Bmatrix}, \\ \boldsymbol{\varepsilon}^s &= \begin{Bmatrix} 2\varepsilon_{31} \\ 2\varepsilon_{23} \end{Bmatrix} = \begin{Bmatrix} \frac{\partial w}{\partial x_1} - \beta_1 \\ \frac{\partial w}{\partial x_2} - \beta_2 \end{Bmatrix},\end{aligned}\quad (2)$$

where $z (=x_3)$ ($|z| \leq t/2$) is coordinate of the plate thickness direction. When an isotropic elastic material is assumed, the stress-strain relation is:

$$\boldsymbol{\sigma} = \mathbf{D}\boldsymbol{\varepsilon}, \quad (3)$$

where $\boldsymbol{\sigma}$ is vector form of the stress components. It is written as, $\boldsymbol{\sigma} = \{\sigma_{11} \ \sigma_{22} \ \sigma_{12} \ \sigma_{23} \ \sigma_{31}\}^T$. \mathbf{D} is an elastic matrix for a shear-deformable plate, given by:

$$\mathbf{D} = \frac{E}{(1-\nu^2)} \begin{bmatrix} 1 & \nu & 0 & 0 & 0 \\ \nu & 1 & 0 & 0 & 0 \\ 0 & 0 & \frac{1-\nu}{2} & 0 & 0 \\ 0 & 0 & 0 & \kappa \frac{1-\nu}{2} & 0 \\ 0 & 0 & 0 & 0 & \kappa \frac{1-\nu}{2} \end{bmatrix}. \quad (4)$$

E , ν and κ are the Young's modulus, Poisson's ratio and the shear correction factor, respectively. $\kappa = \pi^2/12$ is chosen [51].

By using the principle of virtual work, the equilibrium equation for a shear-deformable plate without a gravity force term yields:

$$\int_{\Omega} \delta \boldsymbol{\varepsilon}^T \mathbf{D} \boldsymbol{\varepsilon} \, d\Omega + \int_{\Gamma} \delta \boldsymbol{\beta}^T \bar{\mathbf{m}} \, d\Gamma - \int_{\Omega} \delta w \, p \, d\Omega = 0, \quad (5)$$

where $\boldsymbol{\beta} = \{\beta_1 \ \beta_2\}^T$ is vector form of the deflection angles. $\bar{\mathbf{m}} = \{\bar{m}_1 \ \bar{m}_2\}^T$ denotes a vector for the prescribed moments applied to the plate edges. p is the distributed pressure acting on the plate. δ represents the variational operator.

The moment and shear force components $\mathbf{M} = \{M_{11} \ M_{22} \ M_{12}\}^T$ and $\mathbf{Q} = \{Q_1 \ Q_2\}^T$ based on the vector forms of the strain components $\boldsymbol{\varepsilon} = \{\boldsymbol{\varepsilon}^b \ \boldsymbol{\varepsilon}^s\}^T$ and elastic constants \mathbf{D} , have the form:

$$\begin{Bmatrix} M_{11} \\ M_{22} \\ M_{12} \\ Q_1 \\ Q_2 \end{Bmatrix} = \int_{-t/2}^{t/2} \mathbf{D} \begin{Bmatrix} z \boldsymbol{\varepsilon}^b \\ \boldsymbol{\varepsilon}^s \end{Bmatrix} dz. \quad (6)$$

The three-point Newton-Cotes quadrature rule is employed for numerically integrating the plate thickness direction of Eq.(6).

2.2 RK discretization

The meshfree approximation for field variables in the Mindlin-Reissner plate is presented. The nodes \mathbf{x}_I ($I=1, 2, \dots, \text{NP}$) are distributed on the mid-plane S as shown in Fig.1b. The deflection and deflection angles at point \mathbf{x} are $w(\mathbf{x})$, $\beta_1(\mathbf{x})$ and $\beta_2(\mathbf{x})$, respectively. Each node has three degrees of freedom; i.e., w_I , β_{1I} and β_{2I} for the I -th node. For simple explanation, the physical values and degrees of freedom are represented as $d_i(\mathbf{x})$ and d_{iI} . The subscript i ($=1, 2, 3$) corresponds to the deflection and deflection angles.

The RK is employed as a meshfree interpolant, and the deflection and deflection angles at position \mathbf{x} are represented by the sum of the RKs as:

$$\mathbf{d}^h(\mathbf{x}) = \sum_{I=1}^{\text{NP}} \Psi_I(\mathbf{x}) \mathbf{d}_I, \quad (7)$$

where $\mathbf{d}^h(\mathbf{x}) = \{d_1^h(\mathbf{x}) \ d_2^h(\mathbf{x}) \ d_3^h(\mathbf{x})\}$ is the approximated value vector and $\mathbf{d}_I = \{d_{1I} \ d_{2I} \ d_{3I}\}$ is the coefficient vector. $\Psi_I(\mathbf{x})$ gives the RKs of the I -th node and is expressed as:

$$\Psi_I(\mathbf{x}) = \mathbf{H}^T(\mathbf{x}_I - \mathbf{x}) \mathbf{b}(\mathbf{x}) \phi_{aI}(\mathbf{x}_I - \mathbf{x}), \quad (8)$$

where $\mathbf{H}(\mathbf{x})$, $\mathbf{b}(\mathbf{x})$ and $\phi_{aI}(\mathbf{x})$ are the basis vector, coefficient vector and original kernel function, respectively. A complete quadratic basis is chosen as the basis vector to impose the Kirchhoff mode reproducing condition (Wang and Chen [33], [42]; Sadamoto et al. [35]) as:

$$\mathbf{H}(\mathbf{x}) = \{1 \ x_1 \ x_2 \ x_1^2 \ x_1 x_2 \ x_2^2\}. \quad (9)$$

This condition is necessary to address the shear locking problem in the meshfree plate bending formulation. Additionally, a cubic spline function is taken as the original kernel function $\phi_{aI}(\mathbf{x})$ in Eq.(8):

$$\phi_{aI}(\mathbf{x}_I - \mathbf{x}, h_I) = \frac{10}{7\pi h_I^2} \begin{cases} 1 - \frac{3}{2}s_I^2 + \frac{3}{4}s_I^3 & (0 \leq s_I \leq 1) \\ \frac{1}{4}(2 - s_I)^3 & (1 \leq s_I \leq 2) \\ 0 & (2 \leq s_I) \end{cases}, \quad (10)$$

where $s_I (= \|\mathbf{x}_I - \mathbf{x}\|/h_I)$ is the normalized distance from the center of the kernel function, and h_I is a parameter that controls the functional support size.

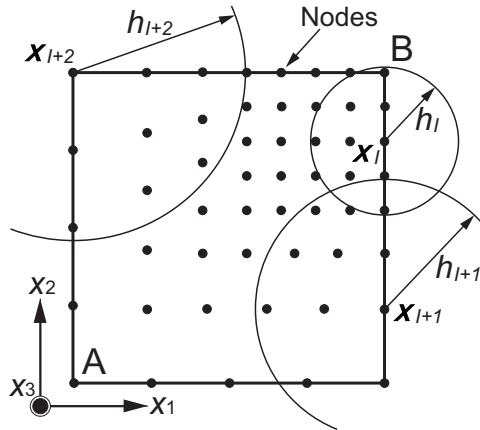


Fig. 2 Control of the nodal density with parameter h_I^p in meshfree modeling

When analyzing a crack whose size is small compared with the problem domain, meshfree modeling often requires controlling the nodal density for the purpose of efficient and high accuracy computations. A schematic illustration of meshfree models with an inclined scattered nodal distribution is shown in Fig.2. The nodal density gradually increases from node A to node B. A control parameter α_I is introduced in h_I (i.e., $h_I (= \alpha_I h_I^p)$), and the RKs are developed so as to satisfy the Kirchhoff mode reproducing condition. α_I is set to be constant for a uniformly distributed model. h_I^p is the characteristic length of the I -th node, which determines the node distance between the I -th node and its neighbors. The normalized distance s_I is gradually varied as the node density changes from node A to node B.

2.3 Crack modeling

Meshfree crack modeling was presented by Tanaka et al. [49-50]. The modeling is briefly reviewed here. A through crack embedded in a plate shown in Fig.1 is considered. A crack tip is represented by a node, and a crack segment ∂S_c is modeled as an assembly of nodes. x'_1 and x'_2 are local coordinates from the crack tip, and (r', θ') denotes a position in the local polar coordinate system. In representing the displacement discontinuity along the crack segment, the RKs across the segment are completely/partially cut. A diffraction method and visibility criterion (Organ et al. [36]; Krysl and Belytschko [37]) are introduced to modify the shapes of RKs. An enriched basis is included in the RKs to accurately capture the severe stress concentration around the crack tip according to the literature (Fleming et al. [38]; Joyot et al. [39]).

A schematic illustration of the crack modeling with RKs is represented in Fig.3. S_+/S_- denotes upper/lower regions of the crack. \mathbf{x}_c is a crack tip node. A diffraction method is adopted to represent the displacement discontinuity, and to improve the accuracy of the fracture mechanics parameter evaluations. When including the crack tip node \mathbf{x}_c within the function support of the node \mathbf{x}_I , the diffraction method is adopted. The RKs are modified so as to wrap around the crack tip node. The normalized distance s_I in the original kernel $\phi_{aI}(\mathbf{x})$ of Eq.(10) is modified as \hat{s}_I to represent the displacement discontinuity across the crack segment:

$$\hat{s}_I = \left(\frac{s_1 + s_2(\mathbf{x})}{s_0(\mathbf{x})} \right)^\lambda \frac{s_0(\mathbf{x})}{h_I}, \quad (11)$$

where $s_0(\mathbf{x}) = \|\mathbf{x} - \mathbf{x}_I\|$, $s_1 = \|\mathbf{x}_c - \mathbf{x}_I\|$, and $s_2(\mathbf{x}) = \|\mathbf{x} - \mathbf{x}_c\|$ are normalized distances presented in Eq.(10). The shape factor λ is set to be unity.

When a crack segment completely crosses the RKs, double nodes are created along the segment. A visibility criterion is adopted for the RKs to represent the displacement discontinuity in the meshfree modeling. The RK is divided into two parts S_+ and S_- across the segment. If a node \mathbf{x}_J belongs to domain S_+ , numerical integration of the stiffness matrix in terms of node \mathbf{x}_J is partially carried out for domain S_+ as shown in Fig.3.

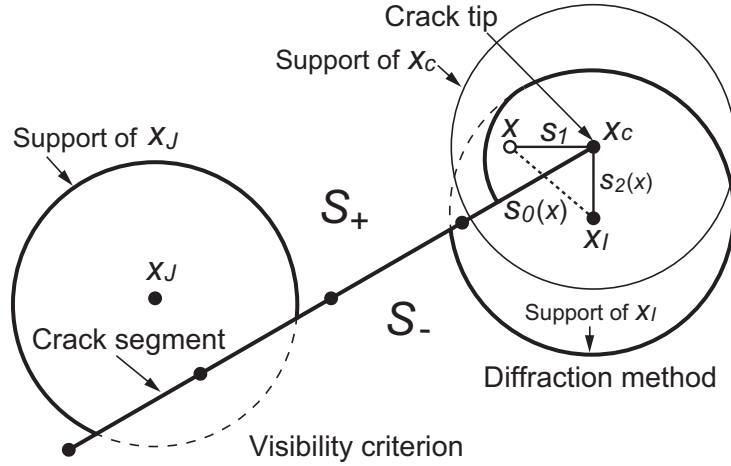


Fig. 3 Modification of the RKs for meshfree crack modeling employing the diffraction method and visibility criterion

An enriched basis is included in the basis vector $\mathbf{H}(\mathbf{x})$ in Eq.(9) to effectively approximate the severe stress concentration around the crack tip. When making an RK around the crack tip, an enriched basis for representing asymptotic crack tip fields is introduced in the basis vector:

$$\mathbf{H}(\mathbf{x}) = \{1 \ x_1 \ x_2 \ x_1^2 \ x_1x_2 \ x_2^2 \ \sqrt{r'} \sin(\theta'/2)\}, \quad (12)$$

where (r', θ') is the local polar coordinate from the crack tip as shown in Fig.1a. The enriched basis vector is only adopted for the quadrature points within the function support of \mathbf{x}_c .

2.4 Nodal integration techniques

In solving the Galerkin formulation in Eq.(5), a numerical integration technique, as well as the fracture mechanics parameter evaluations, is needed to fulfill the internal and external force terms. The physical values $d_j(\mathbf{x})$ and $d_{j,k}(\mathbf{x})$ are smoothed by means of SCNI and SSCI, and their physical values, i.e., $\tilde{d}_j(\mathbf{x})$ and $\tilde{d}_{j,k}(\mathbf{x})$ are thus derived. Here, the nodal integration techniques are briefly summarized.

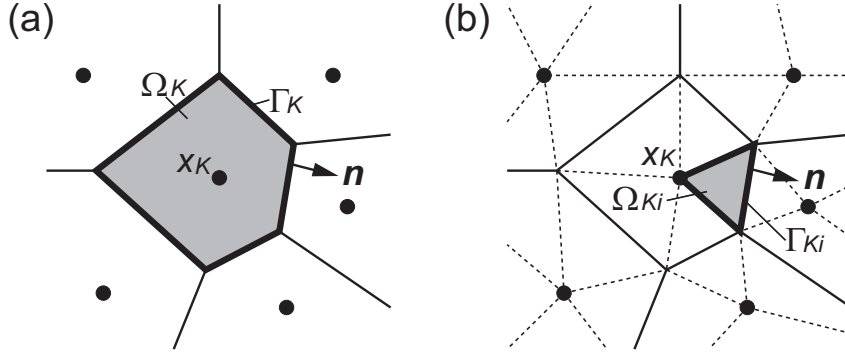


Fig. 4 Nodal integration techniques: **a** SCNI, **b** SSCI

A Voronoi cell diagram and the nodal integration technique are represented in Fig.4a. The physical values $d_j(\mathbf{x})$ ($j= 1, 2, 3$) are smoothed throughout the Voronoi cell, i.e.,

$$\begin{aligned}\tilde{d}_j^h(\mathbf{x}_K) &= \frac{1}{A_K} \int_{\Omega_K} d_j^h(\mathbf{x}) d\Omega \\ &= \sum_{I=1}^{\text{NP}} \frac{1}{A_K} \int_{\Omega_K} \Psi_I(\mathbf{x}) d_{jI} d\Omega,\end{aligned}\quad (13)$$

where $(\tilde{})$ represents a smoothed physical quantity. The physical value $\tilde{d}_j^h(\mathbf{x})$ is averaged over the entire domain Ω_K , and the values are evaluated at node \mathbf{x}_K . A_K is the area of domain Ω_K as shown in Fig.4a.

The derivatives $d_{j,k}(\mathbf{x})$ ($k=1, 2$) are smoothed within a Voronoi cell employing SCNI. The surface integration form of the derivatives is transformed into a line integration form according to the Gauss divergence theorem:

$$\begin{aligned}\tilde{d}_{j,k}^h(\mathbf{x}_K) &= \frac{1}{A_K} \int_{\Omega_K} d_{j,k}^h(\mathbf{x}) d\Omega \\ &= \frac{1}{A_K} \int_{\Gamma_K} d_j^h(\mathbf{x}) n_k d\Gamma \\ &= \sum_{I=1}^{\text{NP}} b_{Ik}(\mathbf{x}_K) d_{jI},\end{aligned}\quad (14)$$

$$b_{Ik}(\mathbf{x}_K) = \frac{1}{A_K} \int_{\Gamma_K} \Psi_I(\mathbf{x}) n_k d\Gamma, \quad (15)$$

where Γ_K is the boundary of a Voronoi cell and n_k denotes the normal to the boundary as shown in Fig.4a.

In crack modeling, SSCI is employed to capture both the severe stress concentration near the crack tip and displacement discontinuity along the crack segment, as well as to evaluate the J -integral. The Voronoi cell in Fig.4a is further divided into a number of triangular subdomains Ω_{K_i} as shown

in Fig.4b. A physical value $\tilde{d}_j^h(\mathbf{x}_{K_i})$ is then approximated by:

$$\begin{aligned}\tilde{d}_j^h(\mathbf{x}_{K_i}) &= \frac{1}{A_{K_i}} \int_{\Omega_{K_i}} d_j^h(\mathbf{x}) d\Omega \\ &= \sum_{I=1}^{\text{NP}} \frac{1}{A_{K_i}} \int_{\Omega_{K_i}} \Psi_I(\mathbf{x}) d_{jI} d\Omega,\end{aligned}\quad (16)$$

where A_{K_i} and Γ_{K_i} are the area and the boundary of the subdomain Ω_{K_i} in Fig.4b. The value is averaged within Ω_{K_i} and is evaluated at the gravity center of the subdomain. The derivatives of the physical components $\tilde{d}_{j,k}^h(\mathbf{x}_{K_i})$ are evaluated through the following expressions:

$$\tilde{d}_{j,k}^h(\mathbf{x}_{K_i}) = \sum_{I=1}^{\text{NP}} b_{Ik}(\mathbf{x}_{K_i}) d_{jI}, \quad (17)$$

$$b_{Ik}(\mathbf{x}_{K_i}) = \frac{1}{A_{K_i}} \int_{\Gamma_{K_i}} \Psi_I(\mathbf{x}) n_k d\Gamma. \quad (18)$$

The smoothed operation in Eq.(18) is called the SSCI. A five point Gauss quadrature rule is adopted to numerically integrate each segment of the domain Ω_K and subdomain Ω_{K_i} .

When evaluating the shear strain of the meshfree Mindlin-Reissner formulation in Eq.(2), the nodal integration technique in Eqs.(13) or (16) is also applied as in Tanaka et al. [50]. The Voronoi cell represented in Fig.4a is divided into a number of triangular subdomains, and a 13-point Gauss quadrature rule is taken for each subdomain to evaluate the surface integration.

By applying the SCNI/SSCI to the meshfree discretization, the displacement-strain relationship of the shear-deformable plate can thus be derived according to the smoothed \mathbf{B} -matrix as:

$$\tilde{\boldsymbol{\varepsilon}}^h = \sum_{I=1}^{\text{NP}} \tilde{\mathbf{B}}_I \mathbf{d}_I, \quad \tilde{\mathbf{B}}_I = \begin{bmatrix} 0 & -zb_{I1} & 0 \\ 0 & 0 & -zb_{I2} \\ 0 & -zb_{I2} & -zb_{I1} \\ b_{I1} & -b_I & 0 \\ b_{I2} & 0 & -b_I \end{bmatrix}. \quad (19)$$

The smoothed strain components $\tilde{\boldsymbol{\varepsilon}}$ can be evaluated using the Voronoi cells or subdomains. The smoothed displacement, strain and stress components are introduced for the virtual work principle in Eq.(5). The discretization form can be evaluated. In this study, the essential boundary condition is treated by using a penalty technique, which has already detailed in Tanaka et al. [50].

3 Evaluation of mixed-mode intensity factors

3.1 J -integral for Mindlin-Reissner plate theory

We consider a through crack embedded in a plate as shown in Fig.1. The local coordinate system x'_1 - x'_2 is taken from the crack tip. The x'_1 -direction is set parallel to the crack. The crack tip region and the contour integral are represented in Fig.5a. ds is a segment of the contour Γ_{Jint} . A path-independent integral in a Mindlin-Reissner plate has been proposed (Sosa and Eischen [52]; Sosa and Herrmann [53]). When the traction on the crack face and the pressure distribution on the plate are neglected, the J -integral components can be written as:

$$J_k = \int_{\Gamma_{\text{Jint}}} \{W \delta_{kj} - (M'_{ij} \beta'_{i,j} + Q'_j w'_{,k})\} n'_j ds, \quad (20)$$

where J_k ($k=1, 2$) denotes the J -integral values for x'_k -directions. δ_{kj} is the Kronecker delta, and $(\)'$ denotes physical values evaluated in the local coordinate system as shown in Fig.5b. n'_j is the normal to the contour. The strain energy density W in the shear-deformable plate is written, as:

$$W = \frac{1}{2} \{M'_{ij} \beta'_{i,j} + Q'_j (\beta'_j + w'_{,j})\}. \quad (21)$$

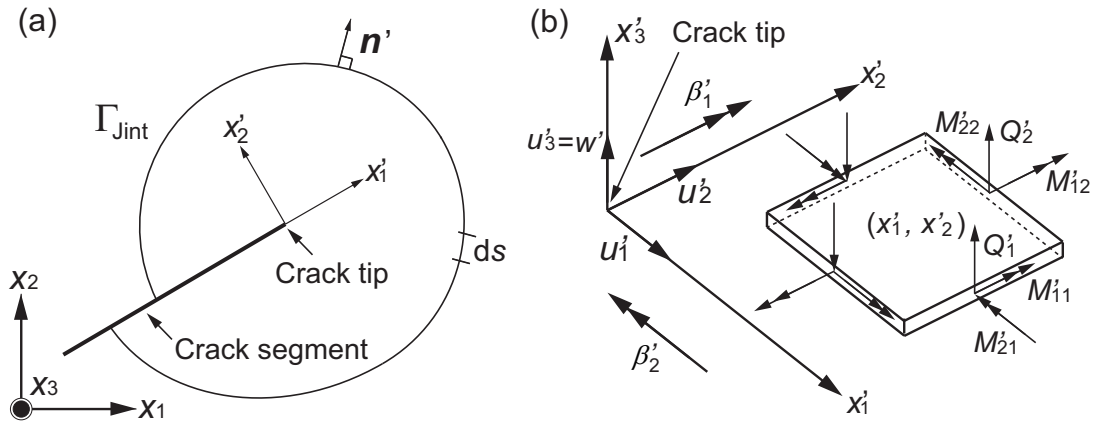


Fig. 5 J -integral for a cracked shear-deformable plate: **a** a contour integral, **b** definition of the physical values based on the local coordinate system x'_1 - x'_2

In the Mindlin-Reissner plate formulation, there are three moment/shear force intensity factors, namely K_1 , K_2 and K_3 . They correspond to symmetric moment M_{22} , asymmetric moment M_{12} and shear force Q_2 as shown in Figs.6a, b and c, respectively, and are expressed as:

$$K_1 = \lim_{r' \rightarrow 0} \sqrt{2r'} M'_{22}(r', 0), \quad (22)$$

$$K_2 = \lim_{r' \rightarrow 0} \sqrt{2r'} M'_{12}(r', 0), \quad (23)$$

$$K_3 = \lim_{r' \rightarrow 0} \sqrt{2r'} Q'_2(r', 0). \quad (24)$$

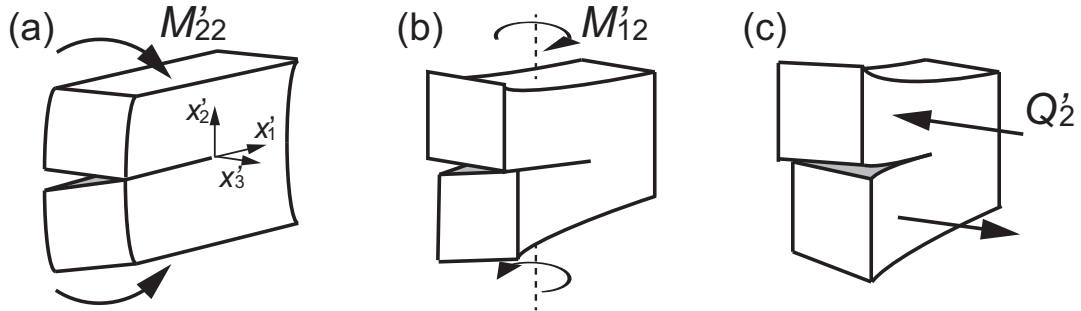


Fig. 6 The moment and shear force intensity factors for a cracked shear-deformable plate: **a** symmetric bending mode K_1 , **b** asymmetric bending mode K_2 , **c** shear mode K_3

The relation between the intensity factors and J -integral value J_1 can be written as:

$$J_1 = \frac{12\pi}{Et^3} \left\{ K_1^2 + K_2^2 + \frac{t^2}{10}(1 + \nu)K_3^2 \right\}. \quad (25)$$

3.2 Mode-splitting of the mixed-mode intensity factors

To decompose the J -integral value J_1 into mixed-mode moment/shear force intensity factors K_1 , K_2 and K_3 , a decomposition method and a displacement ratio method are employed (Rigby and

Aliabadi [48]; Dirgantara and Aliabadi [30]). The J -integral value J_1 is thus separated into symmetric/asymmetric parts, as:

$$J_1 = J_1^S + J_1^{AS}, \quad (26)$$

where J_1^S and J_1^{AS} are the symmetric and asymmetric J -integral values. Decomposition is used to evaluate the symmetric/asymmetric J -integral values. The J -integral value J_1 is decomposed as:

$$J_1^l = \int_{\Gamma_{\text{Jint}}} \{W^l \delta_{1j} - (M_{ij}^l \beta_{i,j}^l + Q_j^l w_{,1}^l)\} n'_j ds, \quad (27)$$

$$W^l = \frac{1}{2} \{M_{ij}^l \beta_{i,j}^l + Q_j^l (\beta_j^l + w_{,j}^l)\}, \quad (28)$$

()^l ($l=S, AS$) of Eqs.(27) and (28) are the smoothed displacement, moment and shear force values for symmetric and asymmetric fields in the local coordinate system ($x'_1-x'_2$).

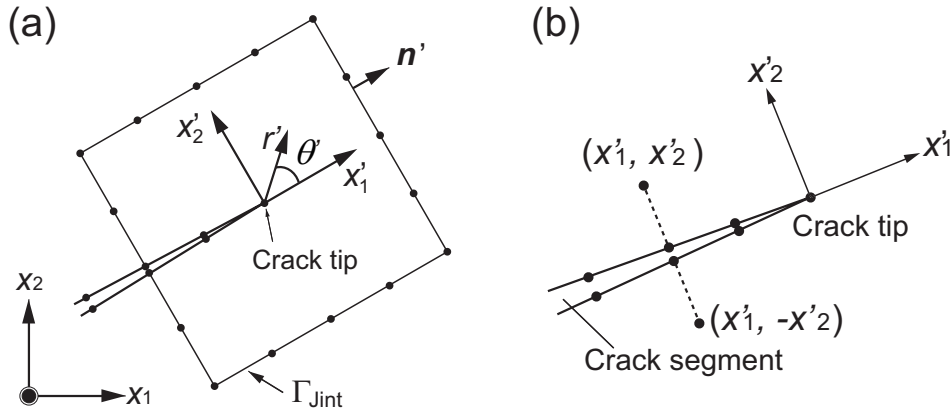


Fig. 7 Evaluation of the contour integral: **a** a rectangular contour, **b** two symmetric points (x'_1, x'_2) and ($x'_1, -x'_2$) across the crack segment

The smoothed displacements, moments and shear forces can be separated using the symmetric/asymmetric parts across the crack segments and the decomposition method. Fig.7a schematically depicts a rectangular contour at a crack tip that is used to evaluate the J -integral values. The physical values are calculated using the two symmetric points (x'_1, x'_2) and ($x'_1, -x'_2$) across the crack segment as shown in Fig.7b:

$$\begin{aligned} \mathbf{u}^S(x'_1, x'_2) &= \begin{Bmatrix} u_1^S(x'_1, x'_2) \\ u_2^S(x'_1, x'_2) \\ u_3^S(x'_1, x'_2) \end{Bmatrix} \\ &= \begin{Bmatrix} u'_1(x'_1, x'_2) + u'_1(x'_1, -x'_2) \\ u'_2(x'_1, x'_2) - u'_2(x'_1, -x'_2) \\ u'_3(x'_1, x'_2) + u'_3(x'_1, -x'_2) \end{Bmatrix}, \end{aligned} \quad (29)$$

$$\begin{aligned} \mathbf{u}^{AS}(x'_1, x'_2) &= \begin{Bmatrix} u_1^{AS}(x'_1, x'_2) \\ u_2^{AS}(x'_1, x'_2) \\ u_3^{AS}(x'_1, x'_2) \end{Bmatrix} \\ &= \begin{Bmatrix} u'_1(x'_1, x'_2) - u'_1(x'_1, -x'_2) \\ u'_2(x'_1, x'_2) + u'_2(x'_1, -x'_2) \\ u'_3(x'_1, x'_2) - u'_3(x'_1, -x'_2) \end{Bmatrix}, \end{aligned} \quad (30)$$

$$\begin{aligned}
\mathbf{M}^S(x'_1, x'_2) &= \begin{Bmatrix} M_{11}^S(x'_1, x'_2) \\ M_{22}^S(x'_1, x'_2) \\ M_{12}^S(x'_1, x'_2) \end{Bmatrix} \\
&= \begin{Bmatrix} M'_{11}(x'_1, x'_2) + M'_{11}(x'_1, -x'_2) \\ M'_{22}(x'_1, x'_2) + M'_{22}(x'_1, -x'_2) \\ M'_{12}(x'_1, x'_2) - M'_{12}(x'_1, -x'_2) \end{Bmatrix}, \tag{31}
\end{aligned}$$

$$\begin{aligned}
\mathbf{M}^{AS}(x'_1, x'_2) &= \begin{Bmatrix} M_{11}^{AS}(x'_1, x'_2) \\ M_{22}^{AS}(x'_1, x'_2) \\ M_{12}^{AS}(x'_1, x'_2) \end{Bmatrix} \\
&= \begin{Bmatrix} M'_{11}(x'_1, x'_2) - M'_{11}(x'_1, -x'_2) \\ M'_{22}(x'_1, x'_2) - M'_{22}(x'_1, -x'_2) \\ M'_{12}(x'_1, x'_2) + M'_{12}(x'_1, -x'_2) \end{Bmatrix}, \tag{32}
\end{aligned}$$

$$\begin{aligned}
\mathbf{Q}^S(x'_1, x'_2) &= \begin{Bmatrix} Q_1^S(x'_1, x'_2) \\ Q_2^S(x'_1, x'_2) \end{Bmatrix} \\
&= \begin{Bmatrix} Q'_1(x'_1, x'_2) + Q'_1(x'_1, -x'_2) \\ Q'_2(x'_1, x'_2) - Q'_2(x'_1, -x'_2) \end{Bmatrix}, \tag{33}
\end{aligned}$$

$$\begin{aligned}
\mathbf{Q}^{AS}(x'_1, x'_2) &= \begin{Bmatrix} Q_1^{AS}(x'_1, x'_2) \\ Q_2^{AS}(x'_1, x'_2) \end{Bmatrix} \\
&= \begin{Bmatrix} Q_1(x'_1, x'_2) - Q_1(x'_1, -x'_2) \\ Q_2(x'_1, x'_2) + Q_2(x'_1, -x'_2) \end{Bmatrix}, \tag{34}
\end{aligned}$$

where $\mathbf{u}^l(x'_1, x'_2)$, $\mathbf{M}^l(x'_1, x'_2)$ and $\mathbf{Q}^l(x'_1, x'_2)$ ($l=S, AS$) are symmetric/asymmetric component vectors for the displacement, moment and shear force, respectively. The separated J -integral values J_1^S and J_1^{AS} can be written with the intensity factors K_1 , K_2 and K_3 as:

$$J_1^S = \frac{12\pi}{Et^3} K_1^2, \tag{35}$$

$$J_1^{AS} = \frac{12\pi}{Et^3} \left[K_2^2 + \frac{t^2(1+\nu)}{10} K_3^2 \right]. \tag{36}$$

In addition, a displacement ratio method (Rigby and Aliabadi [48]; Dirgantara and Aliabadi [30]) is employed to decompose J_1^{AS} of Eq.(36) into K_2 and K_3 . When the displacements near the crack tip correspond to the asymptotic fields of linear fracture mechanics theory, equations can be derived for deflection $\Delta w'$ and deflection angle $\Delta\beta'_1$ along the crack opening according to the local polar coordinate system (r', θ') :

$$\Delta\beta'_1 = \beta'_1(r', +\pi) - \beta'_1(r', -\pi) = \frac{48}{Et^3} \sqrt{2r'} K_2, \tag{37}$$

$$\Delta w' = w'(r', +\pi) - w'(r', -\pi) = \frac{24(1+\nu)}{5Et} \sqrt{2r'} K_3. \tag{38}$$

The ratio between $\Delta\beta'_1$ and $\Delta w'$ can be derived with the intensity factors K_2 and K_3 as:

$$\frac{\Delta\beta'_1}{\Delta w'} = \frac{10}{(1+\nu)t^2} \frac{K_2}{K_3}. \tag{39}$$

Based on the above expressions, J_1^{AS} can further be decomposed in terms of K_2 as:

$$J_1^{AS} = \frac{12\pi}{Et^3} \left[\frac{10}{t^2(1+\nu)} \left(\frac{\Delta w'}{\Delta \beta'_1} \right)^2 + 1 \right] K_2^2, \quad (40)$$

and in terms of K_3 :

$$J_1^{AS} = \frac{12\pi(1+\nu)}{10Et} \left[\frac{t^2(1+\nu)}{10} \left(\frac{\Delta \beta'_1}{\Delta w'} \right)^2 + 1 \right] K_3^2. \quad (41)$$

3.3 J -integral evaluation based on nodal integration

Nodal integration is employed to evaluate the mixed-mode intensity factors of the shear-deformable plate. The contour integral can be calculated by summing the smoothed values in the subdomains and the segments along the rectangular contour. The physical quantities in the meshfree analysis can be used for the J -integral evaluation in the post processing without making a special subroutine for the numerical integration. The meshfree discretization of the contour integral and the mode-splitting technique employing the decomposition and displacement ratio methods are described.

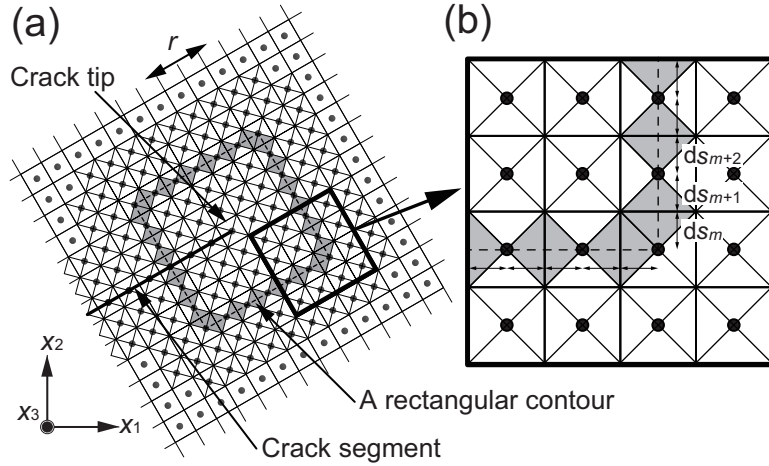


Fig. 8 J -integral discretized by SSCI: **a** a contour integral discretized by the SSCI, **b** close-up view of meshfree discretization for the contour integral

The meshfree discretization of the contour integral is represented in Fig.8a. A rectangular contour $2r \times 2r$ is set to surround the crack tip. SSCI is adopted in the vicinity of the crack tip including the contour to numerically integrate the stiffness matrix and the contour integral. The equally spaced triangular subdomains Ω_{K_i} in Fig.4b are arranged along the contour. The J -integral form in Eqs.(27) and (28) is discretized, as:

$$J_1^l = \sum_{m=1}^{N_{SSCI}} \left(\tilde{W}^l \delta_{1j} - \left[\tilde{M}_{ij}^l \tilde{\beta}_{i,j}^l + \tilde{Q}_j^l \tilde{w}_{,1}^l \right] \right)_m n'_j ds_m, \quad (42)$$

$$\tilde{W}^l = \frac{1}{2} \left[\tilde{M}_{ij}^l \tilde{\beta}_{i,j}^l + \tilde{Q}_j^l (\tilde{\beta}_j^l + \tilde{w}_{,j}^l) \right]_m, \quad (43)$$

where ds_m is a segment of the contour divided by the subdomains as shown in Fig.8b. N_{SSCI} is the number of subdomains along the contour. Additionally, $(\tilde{\cdot})$ signifies smoothed physical quantities. The displacements and their derivatives are evaluated using Eqs.(16) and (18). The moment and shear forces are evaluated through the relations of Eq.(6) and the smoothed \mathbf{B} -matrix in Eq.(19).

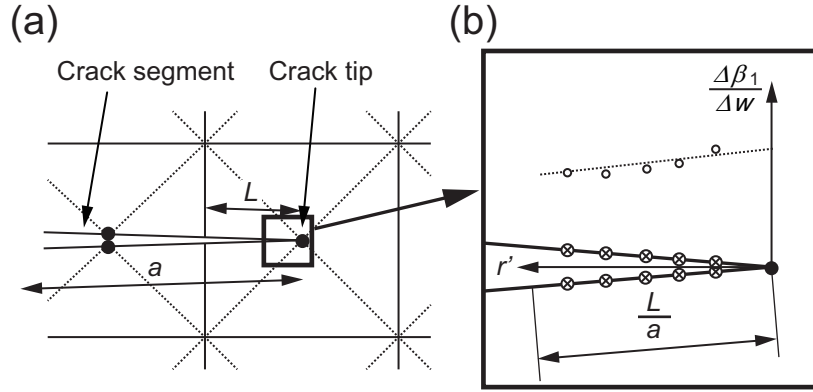


Fig. 9 Schematic of the displacement extrapolation technique used in meshfree analysis: **a** meshfree discretization near the crack tip, **b** evaluation of $\Delta\beta_1'/\Delta w'$ through displacement extrapolation

The moment intensity factor K_1 can be directly calculated from J_1^S according to Eq.(35). Meanwhile, the moment and shear force intensity factors K_2 and K_3 can be evaluated using Eq.(36) and the displacement ratio method based on the relationship of Eqs.(40) and (41). Displacement extrapolation is adopted to evaluate the ratio $\Delta\beta_1'/\Delta w'$. A schematic illustration of meshfree crack modeling around the crack tip is sketched in Fig.9a. The crack tip region is discretized by SSCI, and the width of the subdomain belonging to the crack tip node is denoted L . A close-up view of the region near the crack tip is shown in Fig.9b. It is noted that displacement extrapolation sometime introduces error in the intensity factors. A number of sampling points are placed along the segments $0 < r' < L/a$ on ∂S_c , and the ratio $\Delta\beta_1'/\Delta w'$ is then evaluated at each sampling point. The evaluated value is averaged employing the least-squares method, and is used for mode separation of the moment and shear force intensity factors K_2 and K_3 from J_1^{AS} with the relations of Eqs.(40) and (41).

4 Numerical examples

Several numerical examples of cracked shear-deformable plates are considered, and the evaluated mixed-mode moment/shear force intensity factors are then investigated and discussed to show the accuracy and performance of the proposed meshfree formulation and discretization as well as the J -integral technique. In all numerical examples, the original moment/shear force intensity factors K_i ($i=1, 2, 3$) are transformed through:

$$F_1 = \frac{K_1}{M_0\sqrt{a}}, \quad (44)$$

$$F_2 = \frac{K_2}{M_0\sqrt{a}}, \quad (45)$$

$$F_3 = -\frac{(1+\nu)t}{\sqrt{10}} \frac{K_3}{M_0\sqrt{a}}, \quad (46)$$

where F_i denotes the normalized intensity factors. M_0 is the applied moment and a is the half crack length. t is the plate thickness. A linear elastic material is assumed. The penalty coefficient is set as 1.0×10^7 in all numerical examples.

4.1 Finite plate with a slanted edge crack

A finite rectangular plate including a slanted edge crack is analyzed. The dimensions of the cracked plate are presented in Fig.10a. The plate width is $b=10$ mm, the plate height is $2c=20$ mm, and the plate thickness is $t=5$ mm. The crack length is a and the slant angle is ω . A uniform moment M_0 is applied to the top/bottom edges of the plate. A simply supported condition is applied to the edges.

Young's modulus is $E=210$ GPa and Poisson's ratio is $\nu=0.3$. Liu et al. [54] analyzed the problems employing an infinite element method (Liu and Chiou [55-57]) and used displacement extrapolation to evaluate the moment intensity factor of the cracked shear-deformable plate. Although this is clearly a mixed-mode crack problem, Liu et al. [54] presented only the moment intensity factor K_1 . The numerical results in Liu et al. [54] are digitized and compared with the results of the present study. The path-independent property and accuracy of the moment intensity factor are examined while varying the angle $\omega=\pi/4, 3\pi/8, \pi/2$ rad. and the ratios of the crack length to the plate width $a/b=0.1$ to 0.7.

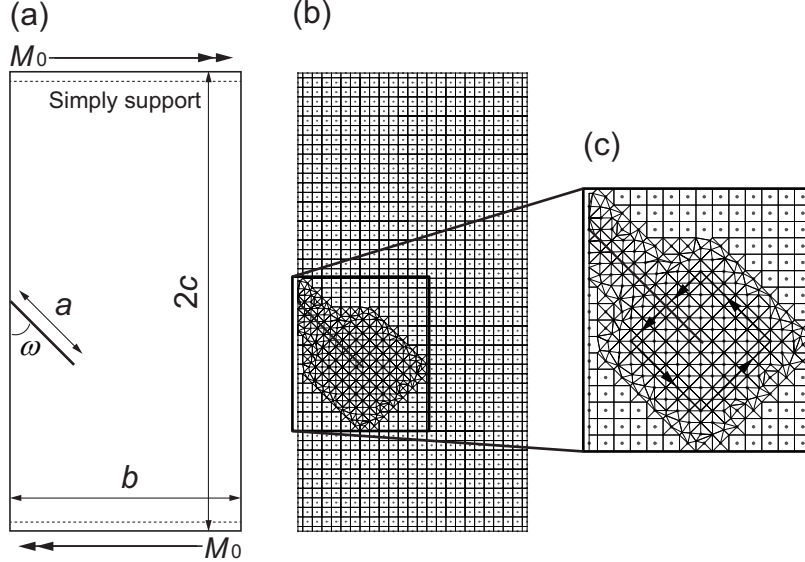


Fig. 10 Slant edge crack in a finite plate: **a** analysis model to be solved, **b** meshfree discretization, **c** close-up view of the region of the crack tip

A meshfree modeling of the cracked plate is represented in Fig.10b. The model is for $\omega=\pi/4$ rad. and $a/b=0.4$. The nodes are distributed on the cracked plate. The node distance along the crack segment ∂S_c is $h_I^p=a/10$. Reproducing kernels are located at each node to approximate the field variables. Voronoi cell diagram is adopted to generate the domain for the nodal integration techniques, i.e., SCNI and SSCI. Stress/strains are smoothed over the whole analysis domain by employing the SCNI, while severe stress concentration near the crack tip can be represented by the SSCI. The meshfree discretization near the crack tip is represented in Fig.10c. A number of rectangular contours are set to evaluate the moment intensity factor in verifying the path-independent property. SSCI with triangular subdomains is adopted to numerically integrate the stiffness matrix and the contour integral around the through crack, while SCNI with the Voronoi cell is applied in the external region of the crack. The parameter of the function support size is $\alpha_I=1.25$ to 1.4 in all cases. J_1^S is evaluated using Eqs.(42) and (43). The moment intensity factor K_1 is calculated from J_1^S using Eq.(35).

The path-independent property is explored first. A normalized moment intensity factor F_1 is analyzed. The obtained numerical results particularly accounted for $a/b=0.4$ are presented in Figs.11a and b for $\omega=\pi/4$ and $3\pi/8$ rad., respectively. Additionally, three node distances along the crack segment ∂S_c are employed for $h_I^p=a/10$, $a/15$ and $a/20$ to examine the accuracy of the intensity factors. The horizontal direction is path r for the contour integral, and the vertical axis is F_1 . The numerical results for $\omega=\pi/4$ and $3\pi/8$ rad. are in good agreement with the reference solutions. The path-independent property can also be found in all cases. It is confirmed that the numerical results converge when $h_I^p \leq a/10$ is employed as observed in Figs.11a and b.

The accuracy of the moment intensity factor is further examined to verify the effectiveness of the meshfree crack modeling and the J -integral evaluation employing SSCI. The slant angles and crack lengths for this investigation are taken as $\omega=\pi/4, 3\pi/8, \pi/2$ rad. and for $a/b=0.1$ to 0.7.

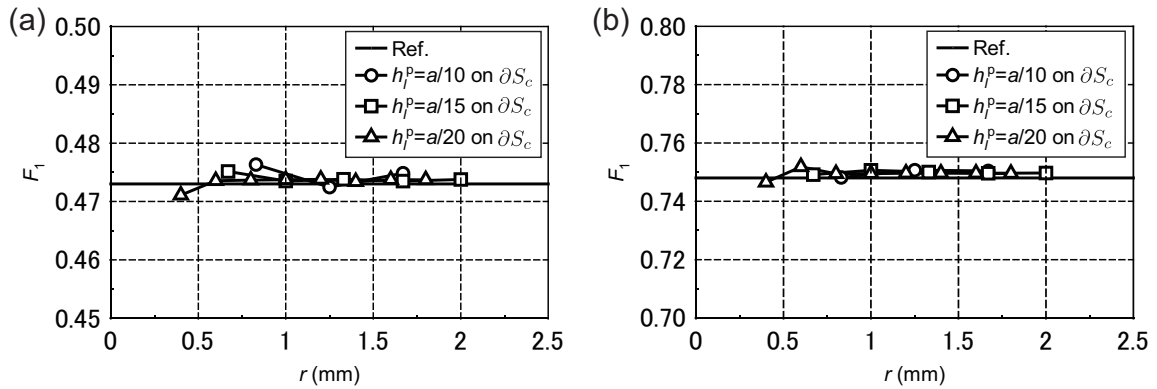


Fig. 11 Comparison of the normalized moment intensity factor F_1 for different contours where the crack length is $a/b=0.4$: **a** $\omega=\pi/4$ rad., **b** $\omega=3\pi/8$ rad. between the present meshfree formulation and the reference method

The meshfree models are generated and F_1 is evaluated. $h_1^p=a/10$ is chosen. The numerical results are then visualized in Fig.12. The open symbols are the numerical results while the lines represent the reference solutions. Importantly, the proposed method offers a good agreement of the normalized moment intensity factor F_1 as compared with the reference solution. It is thus found that the proposed meshfree formulation, discretization and moment intensity factor evaluation employing the nodal integration technique are effective.

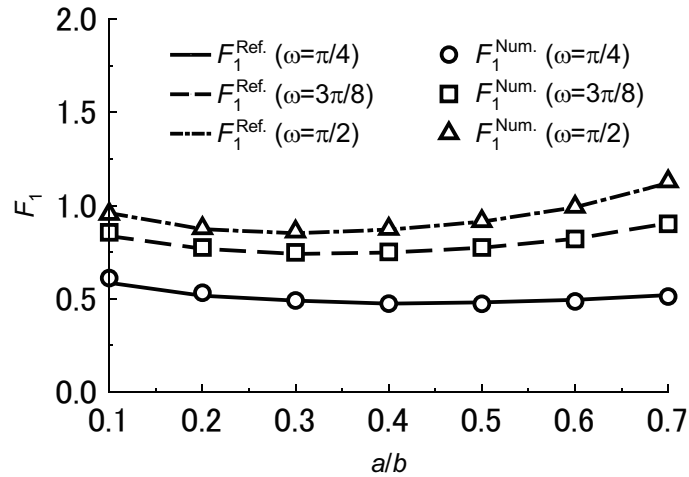


Fig. 12 Normalized moment intensity factor F_1 for $\omega=\pi/4$, $3\pi/8$ and $\pi/2$ rad. for $a/b=0.1$ to 0.7

4.2 Finite plate with an inclined center crack

An inclined center crack in a finite rectangular plate is analyzed. The model geometry and dimensions are depicted in Fig.13a. The width of the plate is $2b=20$ mm, the height is $2c=80$ mm, and the crack length is $2a=1.0$ mm. The angle of inclination is denoted ω . A moment M_0 is applied to top/bottom edges. Additionally, a simply supported boundary condition is applied to the two edges. Young's modulus is $E=200$ GPa. Poisson's ratio $\nu=0.0, 0.25, 0.3$ and 0.5 are chosen. Two reference solutions available in the literature are taken for the comparison purpose, i.e., Sih [28] and Joseph and Erdogan [58] for $\omega=0$ rad., and Sih [28] for $\omega=0$ to $\pi/2$ rad.. Numerical data of the moment intensity factor were presented by Joseph and Erdogan [58] and are employed for the evaluation. The

mixed-mode intensity factors K_1 , K_2 and K_3 are represented by:

$$K_1 = \psi_1 M_0 \sqrt{a} \cos^2(\omega), \quad (47)$$

$$K_2 = \psi_2 M_0 \sqrt{a} \cos(\omega) \sin(\omega), \quad (48)$$

$$K_3 = -\frac{\sqrt{10}}{(1+\nu)t} \psi_3 M_0 \sqrt{a} \cos(\omega) \sin(\omega), \quad (49)$$

where ψ_1 , ψ_2 and ψ_3 are parameters that depend on Poisson's ratio ν and they are determined by an integral equation. The digitized values for $\nu=0.0$, $\nu=0.25/0.3$ and $\nu=0.5$ ($t/a=2.0$) are given in Table 1.

Table 1 Parameters of ψ_1 , ψ_2 and ψ_3 for the reference solutions

ν	ψ_1	ψ_2	ψ_3
0.0	0.77575	0.64592	0.05624
0.25/0.3	0.81171 (0.3)	0.68610 (0.25)	0.06119 (0.25)
0.5	0.83419	0.71734	0.06795

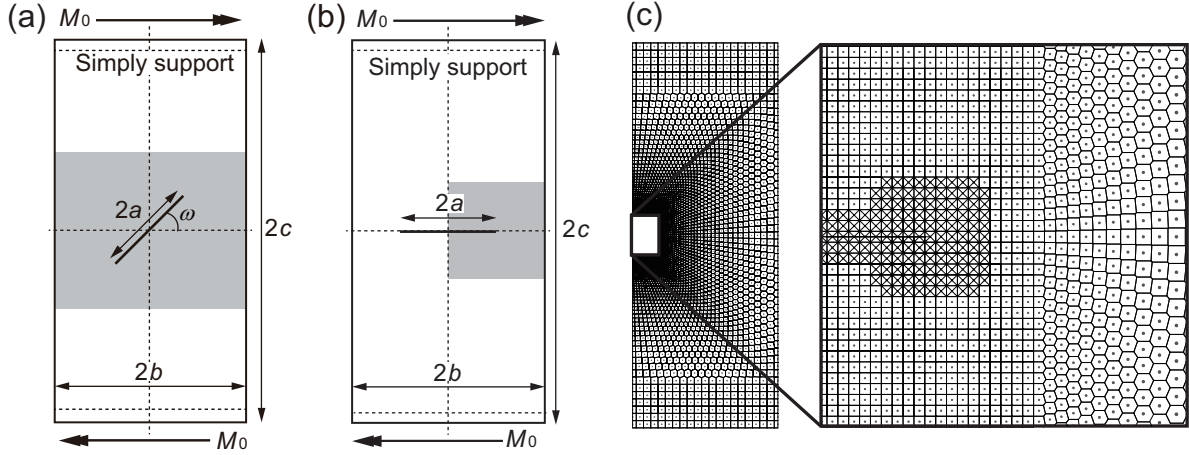


Fig. 13 An inclined center crack in a rectangular finite plate under bending loads: **a** inclined center crack problem, **b** center crack problem ($\omega=0$ rad.), **c** meshfree modeling of a center crack problem ($\omega=0$ rad.)

As a preliminary study of mixed-mode crack problems, the moment intensity factor is analyzed for examination of the convergence, path-independency and accuracy of the present formulation and discretization. The center crack problem as illustrated in Fig.13b is analyzed. The angle of inclination is $\omega=0$ rad.. In the meshfree modeling, only half of the plate is solved because of the symmetrical boundary conditions relating to the symmetry of the problem. The meshfree model of the shaded region in Fig.13b is illustrated in Fig.13c. The node distance along the segment is $h_1^p = a/10$. Because the through crack is much smaller than the whole structure, uniformly distributed nodes are employed around the crack and the node density is gradually changed from the crack region to the external region. The parameter α_l is set with values ranging from 1.25 to 1.4. The whole meshfree model is analyzed by SCNI, and SSCI is applied only to the crack tip and crack segment. Three meshfree models are employed for the node distances $h_1^p = a/10$, $a/15$ and $a/20$ along the crack segment ∂S_c to examine the accuracy of the moment intensity factor. The intensity factor is numerically evaluated using the proposed method and the obtained numerical values are then compared with reference solutions.

The path independency and accuracy of the moment intensity factor are examined first. The normalized intensity factors F_1 are plotted in Figs.14a, b and c for Poisson's ratio $\nu=0.0$, 0.3 and 0.5, respectively. The plate thickness is $t=1.0$; i.e., $t/a=2.0$. F_1 is examined with different contours r .

The intensity factors have almost the same values independent of the path r . Additionally, the results coincide well with the reference solutions given by Sih [28] and Joseph and Erdogan [58]. Additionally, almost the same values are obtained for $h_I^p=a/10$, $a/15$ and $a/20$. It is therefore considered that the moment intensity factor converges at a node density $h_I^p \leq a/10$, as in the previous numerical examples. The node density $h_I^p=a/10$ is chosen for all the following numerical examples.

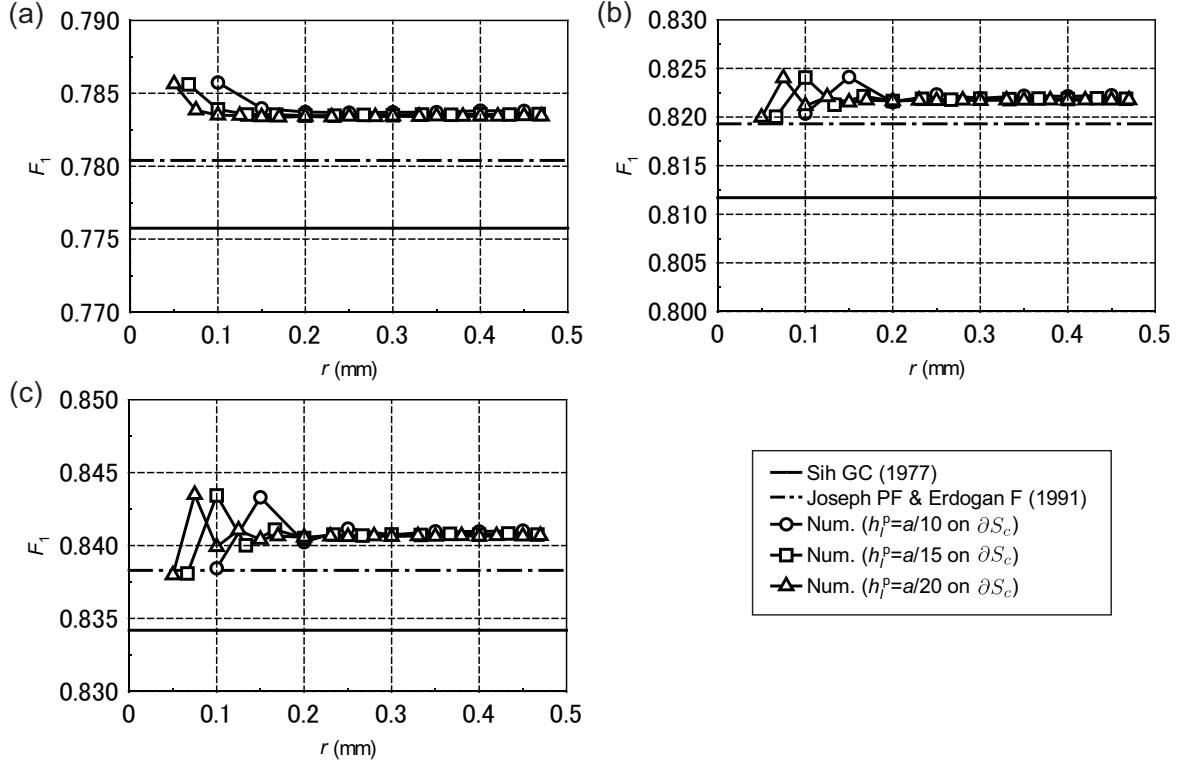


Fig. 14 Comparisons of the normalized moment intensity factor F_1 for various contours of the J -integral evaluation when $t/a=2.0$: **a** $\nu=0.0$, **b** $\nu=0.3$, **c** $\nu=0.5$

To further examine the accuracy of the moment intensity factor, F_1 is examined by changing the ratio of the plate thickness and crack length t/a . The results are represented in Figs.15a and b for t/a for $1.0 \leq t/a \leq 9.0$ and $0.0 \leq t/a \leq 1.0$, respectively. Value of Poisson's ratio $\nu=0.0$, 0.3 and 0.5 are chosen. It is found that F_1 in the meshfree modeling coincides with the reference solutions given by Sih [28] and Joseph and Erdogan [58] for $1.0 < t/a < 9.0$. In addition, the numerical results are in good agreement with the results of Joseph and Erdogan [58] as the plate becomes thinner, while there are deviations between the numerical results and reference solutions of Sih [28] for $0.0 \leq t/a \leq 1.0$.

According to the discussion of the meshfree model for $\omega=0$ rad., an inclined center crack in a finite plate is analyzed. The analysis model is again represented in Fig.13a. The meshfree model of the shaded region of Fig.13a is represented in Fig.16. The angle ω is set to be varied from zero to $\pi/2$ rad.. The meshfree model is for $\omega=\pi/4$ rad. and is discretized for $h_I^p=a/10$ on ∂S_c . The parameter α_I is set from 1.25 to 1.4. The mixed-mode crack problem for $t/a=2.0$ in the case of the Mindlin-Reissner plate was analyzed by Dolbow et al. [18] using the plate formulation. The through crack is modeled using the extended FEM (Moës et al. [19]), and the mixed-mode intensity factors are evaluated using an interaction integral.

Although there are deviations from the reference solutions of Sih [28] when the ratio t/a is less than 1.0, reference solutions of Joseph and Erdogan [58] and the results obtained by the present formulation are in good agreement for $t/a > 1.0$ and the purely mode-I moment intensity factor as shown in Fig.15. Therefore, the plate thickness is set as 1.0; i.e., $t/a=2$ is chosen to verify the mixed-mode fracture problems. The reference solution of Sih [28] is chosen for comparison purposes.

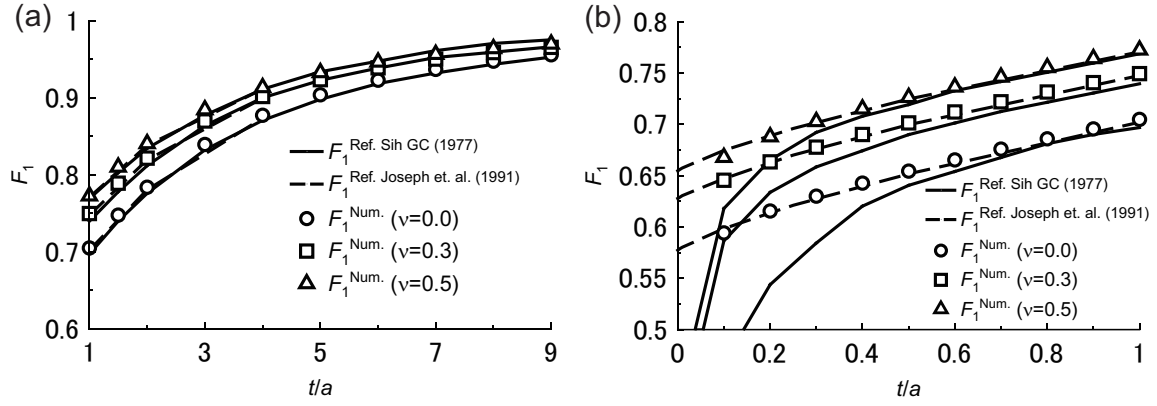


Fig. 15 Normalized moment intensity factor F_1 for various plate thicknesses: a $t/a=1.0-9.0$, b $t/a=0.1-1.0$

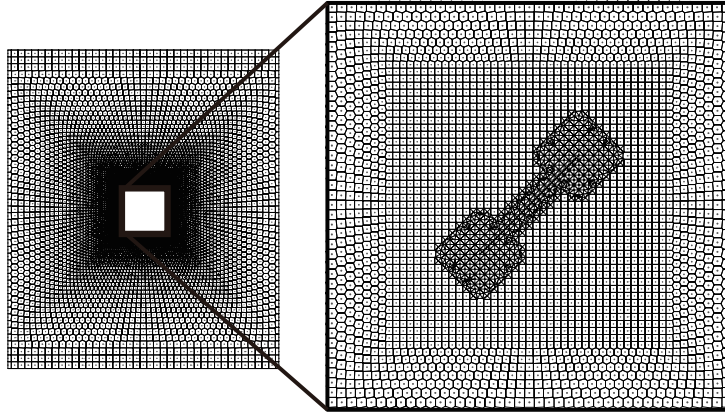


Fig. 16 Meshfree model for an inclined through crack $\omega=\pi/4$ rad.

The normalized moment/shear force intensity factors F_1 , F_2 and F_3 for $\omega=0$ to $\pi/2$ rad. are depicted in Figs.17a, b, and c, respectively. Notice that these numerical results are computed with the parameters that correspond to the Poisson's ratio $\nu=0.0, 0.25/0.3$ and 0.5 , respectively. All numerical results are in good agreement with the reference solutions. To further examine the present approach, the path independency is examined for the mixed-mode intensity factors. The numerical results are then plotted in Figs.18a and b. A crack angle is $\omega=\pi/4$ rad.. Additionally, the node distance is $h_j^p=a/10$. The normalized intensity factors are divided by the reference solutions. All moment/shear force intensity factors have path independency. As a result, it can be concluded that the mixed-mode intensity factors can be effectively evaluated using the proposed contour integral with the decomposition method and the displacement ratio method. In the present study, the moment intensity factor K_1 is evaluated based on an energetic method, while the intensity factors K_2 and K_3 are calculated based on a displacement extrapolation technique. Although a good agreement can be found in the presented numerical results, it is important to note that the accuracy of K_2 and K_3 is deteriorated when the plate thickness decreases. Further research and investigation is needed for the mode separation of K_2 and K_3 .

5 Conclusion

A novel meshfree discretization technique was presented to evaluate mixed-mode moment/intensity factors of a cracked shear-deformable plate. A meshfree Mindlin-Reissner formulation was employed, while the RK particle method was used for meshfree interpolation. A diffraction method, visibility criterion and enriched basis were introduced for the meshfree crack modeling. SCNI/SSCI was used in evaluating the Galerkin formulation. A contour integral was discretized employing nodal integration.

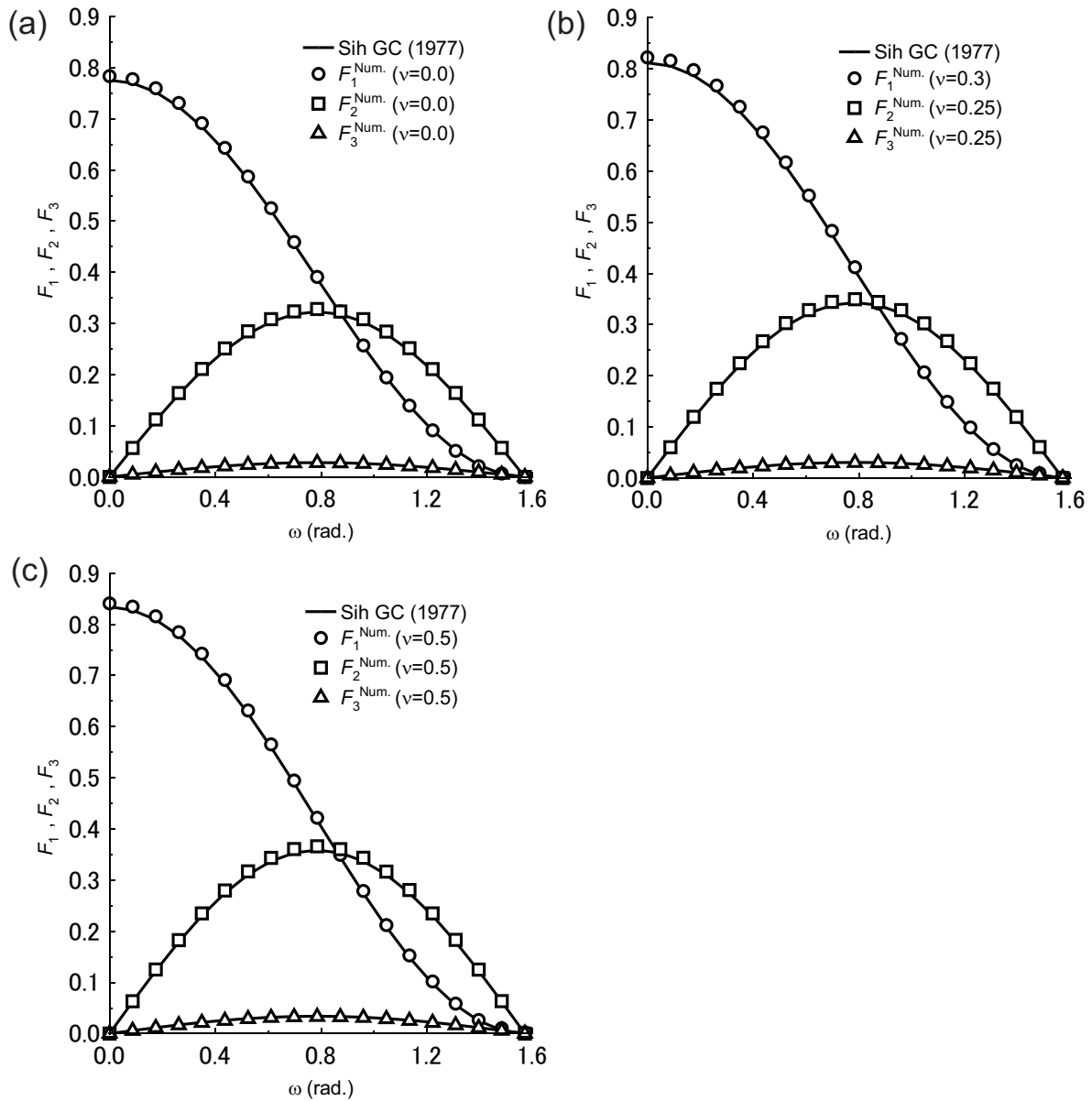


Fig. 17 Normalized SIFs F_1 , F_2 , and F_3 : **a** $\nu=0.0$, **b** $\nu=0.25/0.3$, **c** $\nu=0.5$

A decomposition method and displacement ratio method were employed to separate the J -integral value into mixed-mode intensity factors. The evaluated intensity factors have high accuracy and more interestingly they are path independence, which clearly reveal the effectiveness of the proposed meshfree formulation, crack modeling and discretization in estimating the mixed-mode intensity factors of cracked shear-deformable plates.

Acknowledgements This research was partially supported by the JSPS Grants-in-Aid for Young Scientists (B)(16K18323) and for Scientific Research (A)(15H02328), (B)(15H04212), (B)(16H04603), (C)(15K06632). This work was performed as part of the Cooperative Research Program of the Joining and Welding Research Institute, Osaka University. Tinh Quoc Bui gratefully acknowledges support from Grant-in-Aid for Scientific Research - JSPS. TT Yu gratefully acknowledges support from the National Natural Science Foundation of China (51179063) and the National Sci-Tech Support Plan of China (2015BAB07B10).

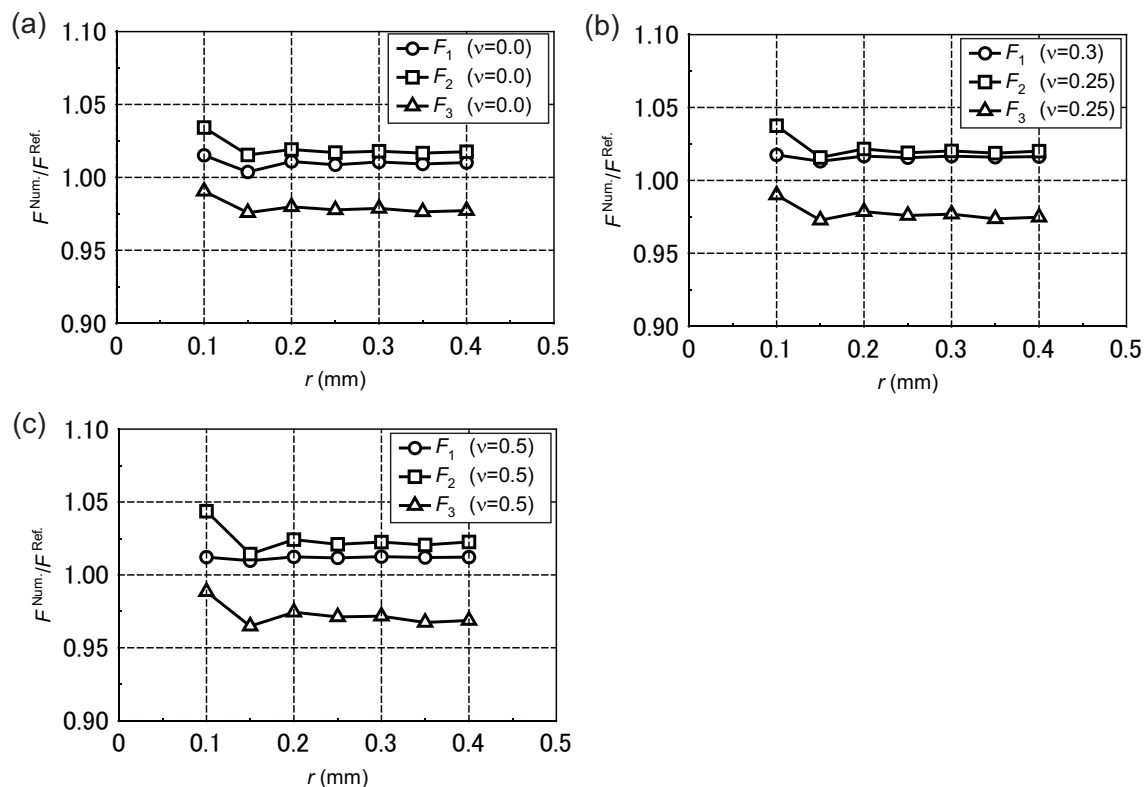


Fig. 18 F_1 , F_2 and F_3 for various paths when the crack angle is $\omega=\pi/4$ rad.: **a** $\nu=0.0$, **b** $\nu=0.25/0.3$, **c** $\nu=0.5$

References

- Maddox, S.J.: Fatigue strength of welded structures, 2nd ed.. Abington Publishing (2002)
- Suresh, S.: Fatigue of materials, 2nd ed.. Cambridge University Press (2002)
- Fricke, W.: Fatigue analysis of welded joints: state of development. Mar. Struct. **16**(3), 185-200 (2003)
- Anderson, T.L.: Fracture mechanics: Fundamentals and applications, 3rd ed.. CRC Press. (2005)
- Toyosada, M., Gotoh, K., Niwa, T.: Fatigue crack propagation for a through thickness crack: a crack propagation law considering cyclic plasticity near the crack tip. Int. J. Fatig. **26**(9), 983-992 (2004)
- Toyosada, M., Gotoh, K., Niwa, T.: Fatigue life assessment for welded structures without initial defects: an algorithm for predicting fatigue crack growth from a sound site. Int. J. Fatig. **26**(9), 993-1002 (2004)
- Okawa, T., Sumi, Y., Mohri, M.: Simulation-based fatigue crack management of ship structural details applied to longitudinal and transverse connections. Mar. Struct. **19**(4), 217-240 (2006)
- Sumi, Y., Nakamura, M., Mohri, M.: Crack paths in weld details under combined normal and shear loading. Eng Fract Mech **77**(11), 2115-2125 (2010)
- He, W., Liu, J., Xie, D.: Numerical study on fatigue crack growth at a web-stiffener of ship structural details by an objected-oriented approach in conjunction with ABAQUS. Mar. Struct. **35**, 45-69 (2014)
- Qiao, W., Sun, J., Xie, D.: Development of super element to perform direct analysis on failure assessment of hull structures based on FAD. Mar. Struct. **39**, 373-394 (2014)
- Yao, T., Fujikubo, M.: Buckling and ultimate strength of ship and ship-like floating structures, 1st ed.. Butterworth-Heinemann (2016)
- Hui, C.Y., Zehnder, A.T.: A theory for the fracture of thin plates subjected to bending and twisting moments. Int. J. Fract. **61**(3), 211-229 (1993)
- Young, M.J., Sun, C.T.: Cracked plates subjected to out-of-plane tearing loads. Int. J. Fract. **60**(1), 1-18, (1993)
- Viz, M.J., Potyondy, D.O., Zehnder, A.T., Rankin, C.C., Riks, E.: Computation of membrane and bending stress intensity factors for thin, cracked plates. Int. J. Fract. **72**(1), 21-38 (1995)
- Su, R.K.L., Leung, A.Y.T.: Mixed mode cracks in Reissner plates. Int. J. Fract. **107**(3), 235-257 (2001)
- Dirgantara, T., Aliabadi, M.H.: Stress intensity factors for cracks in thin plates. Eng. Fract. Mech. **69**(13), 1465-1486 (2002)
- Aliabadi, M.H.: A new generation of boundary element methods in fracture mechanics. Int. J. Fract. **86**(1), 91-125 (1997)
- Dolbow, J., Moës, N., Belytschko, T.: Modeling fracture in Mindlin-Reissner plates with the extended finite element method. Int. J. Solid. Struct. **37**(48-50), 7161-7183 (2000)

19. Moës, N., Dolbow, J., Belytschko, T.: A finite element method for crack growth without remeshing. *Int. J. Numer. Meth. Eng.* **46**(1), 131-150 (1999)
20. Wang, Y.H., Tham, L.G., Lee, P.K.K., Tsui, Y.: A boundary collocation method for cracked plates. *Comput. Struct.* **81**(28-29), 2621-2630 (2003)
21. Zehnder, A.T., Viz, M.J.: Fracture mechanics of thin plates and shells under combined membrane, bending and twisting loads. *Appl. Mech. Rev.* **58**(1), 37-48 (2005)
22. Nguyen-Thanh, N., Valizadeh, N., Nguyen, M.N., Nguyen-Xuan, H., Zhuang, X., Areias, P., Zi, G., Bazilevs, Y., De Lorenzis, L., Rabczuk, T.: An extended isogeometric thin shell analysis based on Kirchhoff-Love theory. *Comput. Meth. Appl. Mech. Eng.* **284**, 265-291 (2015)
23. Hughes, T.J.R., Cottrell, J.A., Bazilevs, Y.: Isogeometric analysis: CAD, finite elements, NURBS, exact geometry and mesh refinement. *Comput. Meth. Appl. Mech. Eng.* **194**(39-41), 4135-4195 (2005)
24. Yu, T.T., Yin, S., Bui, Q.T., Xia, S., Tanaka, S., Hirose, S.: NURBS-based isogeometric analysis of buckling and free vibration problems for laminated composites plates with complicated cutouts using a new simple FSDT theory and level set method. *Thin-Walled Struct.* **101**, 141-156 (2016)
25. Yu, T.T., Bui, Q.T., Yin, S., Doan, D.H., Wu, C.T., Do, T.V., Tanaka, S.: On the thermal buckling analysis of functionally graded plates with internal defects using extended isogeometric analysis. *Compos. Struct.* **136**, 684-695 (2016)
26. Yin, S., Yu, T.T., Bui, Q.T., Zheng, X., Tanaka, S.: In-plane material inhomogeneity of functionally graded plates: A higher-order shear deformation plate isogeometric analysis. *Compos. Part B Eng.* **106**, 273-284 (2016)
27. Yin, S., Yu, T.T., Bui, Q.T., Liu P., Hirose, S.: Buckling and vibration extended isogeometric analysis of imperfect graded Reissner-Mindlin plates with internal defects using NURBS and level sets. *Comput. Struct.* **177**, 23-38 (2016)
28. Sih, G.C. ed.: *Plates and shells with cracks*, Mechanics of Fracture Vol.3. Noordhoff International Publishing (1977)
29. Murakami, Y. ed.: *Stress intensity factors handbook*. Pergamon Press (1987)
30. Dirgantara, T., Aliabadi, M.H.: Crack growth analysis of plates loaded by bending and tension using dual boundary element method. *Int. J. Fract.* **105**(1), 27-47 (2000)
31. Dirgantara, T., Aliabadi, M.H.: Numerical simulation of fatigue crack growth in pressurized shells. *Int. J. Fatig.* **24**(7), 725-738 (2002)
32. Liu, W.K., Jun, S., Zhang, Y.F.: Reproducing kernel particle methods. *Int. J. Numer. Meth. Fluid.* **20**(8-9), 1081-1106 (1995)
33. Wang, D., Chen, J.S.: Locking-free stabilized conforming nodal integration for meshfree Mindlin-Reissner plate formulation. *Comput. Meth. Appl. Mech. Eng.* **193**(12-14), 1065-1083 (2004)
34. Wang, D., Sun, Y.: A Galerkin meshfree method with stabilized conforming nodal integration for geometrically nonlinear analysis of shear deformable plates. *Int. J. Comput. Meth.* **8**(4), 685-703 (2011)
35. Sadamoto, S., Tanaka, S., Okazawa, S.: Elastic large deflection analysis of plates subjected to uniaxial thrust using meshfree Mindlin-Reissner formulation. *Comput. Mech.* **52**(6), 1313-1330 (2013)
36. Organ, D., Fleming, M., Terry, T., Belytschko, T.: Continuous meshless approximations for nonconvex bodies by diffraction and transparency. *Comput. Mech.* **18**(3), 225-235 (1996)
37. Krysl, P., Belytschko, T.: Element-free Galerkin method: Convergence of the continuous and discontinuous shape functions. *Comput. Meth. Appl. Mech. Eng.* **148**(3-4), 257-277 (1997)
38. Fleming, M., Chu, Y.A., Moran, B., Belytschko, T.: Enriched element-free Galerkin methods for crack tip fields. *Int. J. Numer. Meth. Eng.* **40**(8), 1483-1504 (1997)
39. Joyot, P., Trunzler, J., Chinesta, F. Enriched reproducing kernel approximation: Reproducing functions with discontinuous derivatives. *Lecture Notes in Comput. Sci. and Engrg.* **43**, 93-107 (2005)
40. Chen, J.S., Wu, C.T., Yoon, S., You, Y.: A stabilized conforming nodal integration for Galerkin meshfree methods. *Int. J. Numer. Meth. Eng.* **50**(2), 435-466 (2001)
41. Chen, J.S., Yoon, S., Wu, C.T.: Non-linear version of stabilized conforming nodal integration for Galerkin mesh-free methods. *Int. J. Numer. Meth. Eng.* **53**(12), 2587-2615 (2002)
42. Wang, D., Chen, J.S.: A Hermite reproducing kernel approximation for thin-plate analysis with sub-domain stabilized conforming integration. *Int. J. Numer. Meth. Eng.* **74**(3), 368-390 (2008)
43. Wang, D., Lin, Z.: Free vibration analysis of thin plates using Hermite reproducing kernel Galerkin meshfree method with sub-domain stabilized conforming integration. *Comput. Mech.* **46**(5), 703-719 (2010)
44. Wang, D., Lin, Z.: Dispersion and transient analyses of Hermite reproducing kernel Galerkin meshfree method with sub-domain stabilized conforming integration for thin beam and plate structures. *Comput. Mech.* **48**(1), 47-63 (2011)
45. Wang, D., Lin, Z.: A comparative study on the dispersion properties of HRK and RK meshfree approximations for Kirchhoff plate problem. *Int. J. Comput. Meth.* **9**(1), 1240015 (2012)
46. Tanaka, S., Sadamoto, S., Okazawa, S.: Nonlinear thin-plate bending analyses using the Hermite reproducing kernel approximation. *Int. J. Comput. Meth.* **9**(1), 1240012 (2012)
47. Wang, D., Peng, H.: A Hermite reproducing kernel Galerkin meshfree approach for buckling analysis of thin plates. *Comput. Mech.* **51**(6), 1013-1029 (2013)
48. Rigby, R.H., Aliabadi, M.H.: Mixed-mode J-integral method for analysis of 3D fracture problems using BEM. *Eng. Anal. Bound. Elem.* **11**(3), 239-256 (1993)
49. Tanaka, S., Suzuki, H., Sadamoto, S., Sannomaru, S., Yu, T., Bui, Q.T.: J-integral evaluation for 2D mixed-mode crack problems employing a meshfree stabilized conforming nodal integration method. *Comput. Mech.* **58**(2), 185-198 (2016)
50. Tanaka, S., Suzuki, H., Sadamoto, S., Imachi, M., Bui, Q.T.: Analysis of cracked shear deformable plates by an effective meshfree plate formulation. *Eng. Fract. Mech.* **144**, 142-157 (2015)

51. Stephen, N.G.: Mindlin plate theory: Best shear coefficient and higher spectra validity. *J. Sound. Vib.* **202**(4), 539-553 (1997)
52. Sosa, H.A., Eischen, J.W.: Computation of stress intensity factors for plate bending via a path-independent integral. *Eng. Fract. Mech.* **25**(4), 451-462 (1986)
53. Sosa, H., Herrmann, G.: On invariant integrals in the analysis of cracked plates. *Int. J. Fract.* **40**(2), 111-126 (1989)
54. Liu, D.S., Cheng, K.L., Zhuang, Z.W.: Development of plate infinite element method for stress analysis of elastic bodies with singularities. *J Mech* **29**(3), 481-492 (2013)
55. Liu, D.S., Chiou, D.Y.: A coupled IEM/FEM approach for solving elastic problems with multiple cracks. *Int. J. Solid. Struct.* **40**(8), 1973-1993 (2003)
56. Liu, D.S., Chiou, D.Y.: Modeling of inclusions with interphases in heterogeneous material using the infinite element method. *Comput. Mater. Sci.* **31**(3-4), 405-420 (2004)
57. Liu, D.S., Chiou, D.Y.: 2-D infinite element modeling for elastostatic problems with geometric singularity and unbounded domain. *Comput. Struct.* **83**(25-26), 2086-2099 (2005)
58. Joseph, P.F., Erdogan, F.: Bending of a thin Reissner plate with a through crack. *J. Appl. Mech.* **58**(3), 842-846 (1991)